






HEART MODEL FOR ELECTROPHYSIOLOGY, MECHANICS AND BLOOD FLOW

Miljan Milošević^{1,2,3,*}  [0000-0003-3789-2404], Bogdan Milićević^{1,2*}  [0000-0002-0315-8263], Vladimir Simić^{1,2}  [0000-0001-7842-8902], Nenad Filipović^{2,4}  [0000-0001-9964-5615] and Miloš Kojić^{2,5}  [0000-0003-2199-5847]

¹ Institute for Information Technologies, University of Kragujevac, Kragujevac, Serbia
e-mail: miljan.m@kg.ac.rs, vsimic@kg.ac.rs, bogdan.milicevic@uni.kg.ac.rs

² Bioengineering Research and Development Center BioIRC, Kragujevac, Serbia
e-mail: fica@kg.ac.rs, mkojic42@gmail.com

³ Belgrade Metropolitan University, Belgrade, Serbia

⁴ Faculty of Engineering, University of Kragujevac, Kragujevac, Serbia

⁵ Serbian Academy of Sciences and Arts, Belgrade, Serbia

**corresponding author*

Abstract

Cardiovascular diseases are among the leading causes of mortality worldwide, necessitating advanced computational modeling to study their underlying mechanisms and explore potential treatments. In this paper, we present a multiphysics computational model that integrates cardiac mechanics, electrophysiology, and mass transport, implemented within the PAKFIS version of the PAK finite element (FE) code. Our model employs state-of-the-art FE techniques for macroscale fluid-structure interactions in the left ventricle, capturing the complex biomechanical behavior of the heart. For cardiac mechanics, we introduced a FE methodology incorporating standard 3D models and an original shell/membrane FE formulation tailored to the heart's tissue structure. A nonlinear, orthotropic material model for the human heart wall is developed based on experimental investigations of passive myocardium properties. The constitutive behavior is described using Cauchy stress-stretch and shear stress-shear amount relations derived from biaxial extension and triaxial shear experiments. The computational framework determines stresses at FE integration points under various loading conditions. Cardiac contractions are driven by electrical signals propagating through the Purkinje network and myocardial tissue. To model electrophysiology, we apply the smeared physical field methodology (Kojic Transport Model, KTM) to solve electrostatic problems related to cardiac excitation. By coupling cardiac mechanics and electrophysiology, our model provides a comprehensive tool for simulating heart function under physiological and pathological conditions. These advancements contribute to a deeper understanding of cardiac behavior and offer a foundation for future research in cardiovascular disease treatment and prevention.

Keywords: Heart modeling, heart mechanics, electrophysiology, multi-scale modeling, Kojic Transport Model (KTM)

1. Introduction

Cardiovascular diseases are among the most prevalent and life-threatening conditions worldwide. Extensive efforts have been directed toward the development of new drugs, medical research, and computational models that can simulate the cardiac cycle and assess the effects of various factors and therapeutic interventions. Among computational approaches, the finite element method (FEM) has been widely used due to its ability to model complex biomechanical phenomena. A comprehensive cardiac FEM model typically integrates electrophysiology, electro-mechanical coupling, and fluid dynamics to accurately capture the heart's function under both physiological and pathological conditions.

The fundamental processes in the human body are driven and regulated by the nervous system, with electrical signal generation and propagation playing a critical role. In the heart, contractions are initiated by an electrical signal originating from the sinoatrial node (SAN), which propagates through the atria and reaches the atrioventricular node (AVN). The AVN introduces a delay in signal transmission to ensure the sequential contraction of the atria and ventricles. From there, the electrical impulse travels through the Bundle of His, the bundle branches, and the Purkinje fiber network, rapidly distributing excitation signals across the ventricular myocardium. The role of this network is to transfer the electrical signal with high speed to the muscle cells (Zipes et al., 2018). This excitation triggers a change in membrane potential, known as the action potential, which subsequently initiates intracellular calcium signaling and ultimately leads to muscle contraction. The conduction process in Purkinje fibers can be effectively modeled as a 1D phenomenon, embedded in a 3D finite element framework to capture the coupling between electrophysiology and mechanics.

To accurately model heart function, both active and passive stresses must be considered. Active stresses arise from electrical excitation and intracellular calcium dynamics, leading to muscle contraction, while passive stresses depend on the mechanical properties of the myocardium. Mechanical models for muscles rely on the calcium concentration changes within cells (Lafortune et al., 2012; Kim et al., 2010; Hunter et al., 1998; Mijailovich et al., 2010). The structural complexity of the left ventricle, with its helicoidal fiber arrangement, requires an advanced material model capable of capturing orthotropic behavior. Experimental studies, particularly those conducted by Holzapfel and colleagues (Sommer et al., 2015, Holzapfel and Ogden, 2009; McEvoy et al., 2018), have provided valuable insights into the biomechanical properties of the myocardium through biaxial extension and triaxial shear testing. These studies serve as a foundation for constructing a nonlinear, orthotropic material model that characterizes the stress-strain response of cardiac tissue under various loading conditions.

This paper presents a multiphysics computational model integrating electrophysiology, cardiac mechanics, and fluid-structure interaction within the PAKFIS finite element framework. The structure of the paper is as follows: Section 2 introduces the computational modeling of electrophysiology, detailing the mathematical framework for electrical signal propagation through the Purkinje fiber network and extracellular space. Section 3 focuses on the computational modeling of heart mechanics, describing the finite element methodology and the nonlinear material model used for myocardium simulation. Section 4 presents the coupled electro-mechanical model, emphasizing the interaction between electrical excitation, calcium dynamics, and muscle contraction. Finally, Section 5 addresses the coupling of heart wall motion with blood flow, integrating fluid-structure interaction techniques to simulate the left ventricle's biomechanical behavior.

2. Computational modeling of electrophysiology

The finite element (FE) modeling of electrophysiology in the PAK FE code is based on fundamental principles from electrostatics, specifically Ohm's law and the continuity equation for current flux density. These principles serve as the foundation for simulating electrical conduction within cardiac tissue. Ohm's law, first formulated by Georg Ohm in 1827, describes the relationship between voltage, current, and resistance, making it one of the essential laws in physics. The continuity equation for current density, derived from Maxwell's Equations (1873), is incorporated into the finite element framework through an incremental iterative scheme.

In complex biological structures, different tissue domains, such as muscle cells, are often separated by membranes. In the case of 1D domains, such as neural fibers or Purkinje networks, electrical conduction across walls is modeled using cable theory, as described by Winslow (1992). The electrical flux across these walls can be mathematically expressed as:

$$I_m = G_m (V_{in} - V_{out}) + C_m \left(\frac{\partial V_{in}}{\partial t} - \frac{\partial V_{out}}{\partial t} \right) \quad (1)$$

where G_m represents membrane conductivity and C_m denotes the specific membrane capacitance. This formulation reduces the problem of electrical conduction in a continuum to determining a scalar-valued electrical potential function $V_e(x, y, z, t)$, subject to the necessary boundary and initial conditions. In the Purkinje fiber network, signal propagation occurs along cable-like structures, reducing the electrical conduction problem to one dimension. The governing equation for this scenario is derived under the assumption of 1D conduction along the cable, leading to the following transport equations (Kojic et al., 2019):

$$G_a \frac{\partial^2 V_e^{in}}{\partial x^2} = G_m (V_e^{in} - V_e^{ext}) + C_m \left(\frac{\partial V_e^{in}}{\partial t} - \frac{\partial V_e^{ext}}{\partial t} \right) \quad (2)$$

where V_e^{in} and V_e^{ext} represent electrical potentials within the cable and its surrounding medium, respectively; G_a and G_m correspond to conductivities along and across the cable wall; and C_m is the membrane capacitance [Fm^{-2}]. This equation, rooted in the cable theory developed by William Thomson in the 1850s for telegraphic signal decay, forms the basis for electrical conduction modeling in neural fibers and Purkinje networks. The first implementation of this model for simulating electrical transport in neural fibers was introduced in (Kojic et al., 2019), incorporating axial and lateral currents through a composite cable finite element (CCFE) formulation. Axial conduction is modeled using standard 1D finite elements, while electrical transport through cell membranes is captured via a connectivity element. Lateral electrical flow, representing transmission across the surface of the element, is also accounted for.

To validate this methodology, several representative examples were developed. The first case involved a composite 1D FE model for electrical conduction (CCFE), where numerical results were successfully compared against analytical solutions, confirming the model's accuracy. Additionally, a neural network embedded within tissue was simulated (Figure 1a). In this scenario, a square tissue domain (10×10 mm) containing a neural fiber network (depicted in red) was considered. A constant electrical potential was prescribed at two boundaries, while the lateral boundaries were treated as impermeable. The temporal evolution of mean potential in neural fibers and the surrounding tissue showed slight variations between detailed and smeared models (KTM), attributed to potential gradients in both domains.

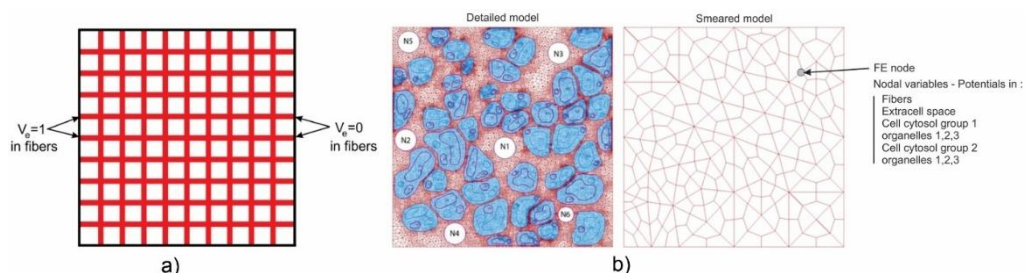


Fig. 1. (a) Square tissue domain (10×10 mm) with neural network (red) interacting with surrounding tissue. Constant electrical potential is prescribed at two boundaries. (b) Tissue domain (50×50 μm) with neural fibers (N1 to N6) oriented perpendicular to the plane. Left: Detailed model with 2D elements. Right: Smeared model (KTM) (according to Kojic et al., 2019).

In a second example (Figure 1b), electrical conduction was coupled with ionic transport, where transported ions generated an electric charge within the tissue. This multiscale modeling approach considered the tissue as a composite medium consisting of neural fibers, different continuum domains, and cell membranes. The computational model included ionic currents across membranes and an isolated 2D tissue region composed of multiple cell groups, each containing three organelles with distinct material properties and volumetric fractions. The detailed model utilized 2D elements to represent both the continuum domains and cellular membranes, while the smeared model incorporated neural fibers, cell domains, and membranes as a unified entity with nodal potentials. Selected scenarios included cases with: constant potential in fibers, a bolus function for fiber potential, an excitation pattern resembling Purkinje fiber activity, and models incorporating potassium and sodium currents. For all investigated cases, the evolution of electric potential over time exhibited a strong correlation between detailed and smeared models across different domains.

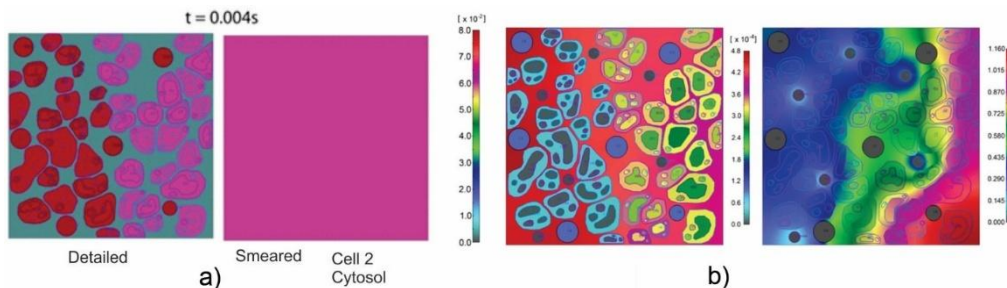


Fig. 2. (a) Electrical potential fields in the presence of ionic currents (potassium and sodium). Left: Detailed model for cell group 2. Right: Smeared model (KTM) (b) Coupled electrical conduction and diffusion. Left: Ionic concentration field at $t = 1\text{s}$. Right: Electrical potential distribution (according to Kojic et al., 2019).

Three tissue models with varying fiber alignments were developed (Figure 3a–c): (a) parallel-aligned fibers, (b) orthogonally arranged fibers, and (c) a combination of orthogonal and diagonal fiber orientations. The mean electrical potential evolution within the tissue showed consistent results for both detailed and smeared models, reinforcing the accuracy of the smeared approach. A 2D heart wall tissue model incorporating Purkinje fibers was also analyzed (Figure 3e, f), further confirming the feasibility of this methodology.

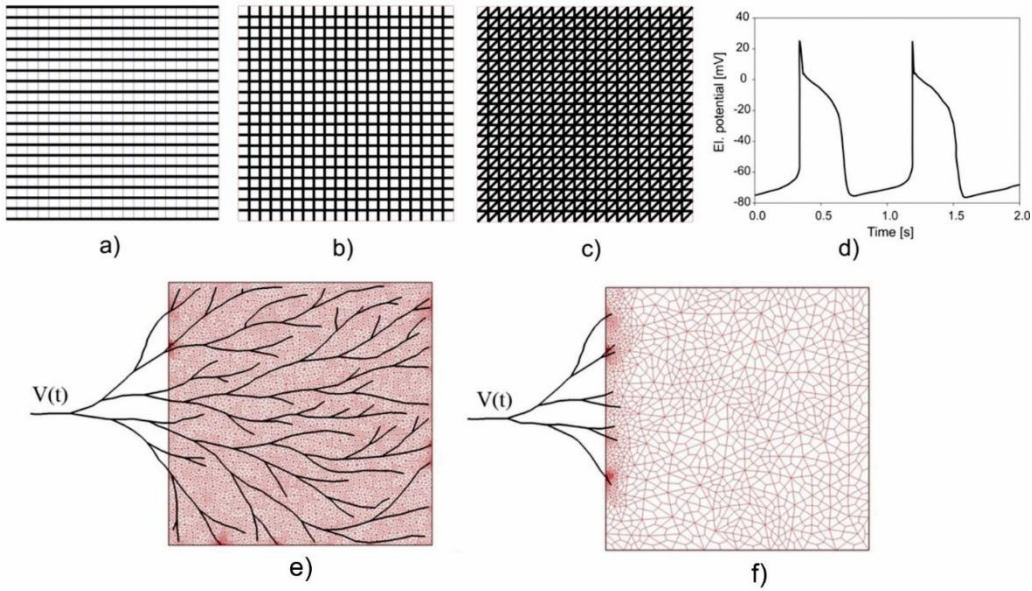


Fig. 3. (a–c) Tissue models with different fiber orientations. (d) Electrical potential in fibers at inlet boundary corresponding to heart cycles, with zero potential at the opposite boundary. (e) Purkinje fiber branching into tissue with prescribed potential. Left: Detailed FE model. (f) Corresponding smeared FE model (KTM) (according to Geroski et al., 2020).

Finally, a 3D biventricular heart model was developed to assess the feasibility of applying the smeared approach to whole-heart simulations (Figure 4). The 3D heart geometry was reconstructed from CT imaging data, and Purkinje fibers were manually embedded as a network of 1D lines on the inner surfaces of the left and right ventricles. The resulting model, which combines a full 1D Purkinje network with a 3D tissue mesh, serves as the detailed representation. To generate a smeared equivalent, an equivalent continuum layer was introduced to replace the explicit 1D Purkinje network. Electrical excitation was initiated at the atrioventricular node (AVN) using a prescribed potential function $V_{in}(t)$. The resulting electrical potential fields at $t=0.75s$ for both detailed and smeared models are shown in Figures 4c and 4d, respectively.

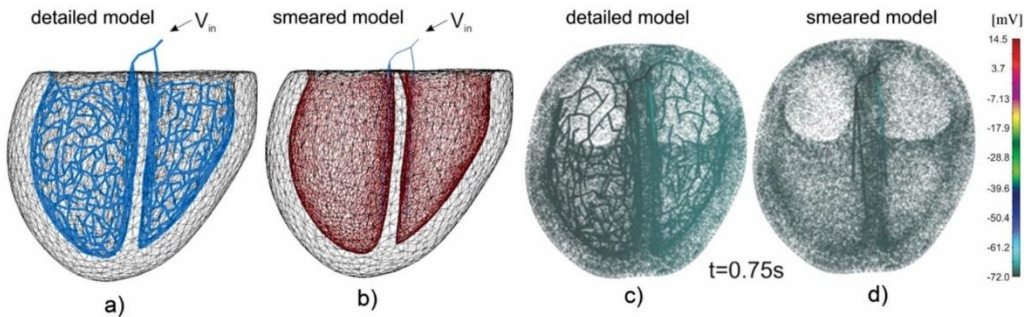


Fig. 4. (a) Detailed model with 1D Purkinje fibers network; (b) Smeared model with Purkinje fibers layer and the surrounding tissue layer. (c) Electrical potential field in tissue for the detailed model, (d) Electrical potential field in tissue for smeared model (KTM) (according to Kojic et al., 2022.).

These examples highlight the robustness of the proposed finite element methodology, demonstrating its applicability for simulating electrophysiology in cardiac tissue. The accuracy and efficiency of the smeared model make it a promising tool for practical applications in cardiac electrophysiology.

3. Computational modeling of heart mechanics

Key continuum mechanics and finite element principles, which incorporate experimental findings, have been implemented in the PAK finite element code and are detailed in (Kojic et al., 2021). The formulation employs velocities as nodal variables, making them particularly suitable for coupling heart wall motion with blood flow. The force-balance equations for a finite element per unit volume are expressed in an incremental-iterative form. Additionally, a computational procedure for stress evaluation, based on Kojic and Bathe (2005) and Bathe (1996), has been developed. Normal stress interpolation is conducted within a local material coordinate system, accounting for different loading conditions. Specifically, interpolation is performed for (A) fiber direction and (B) sheet direction. For the normal direction, experimental sheet stress-strain curves from Stevens et al. (2003) are used, with strain scaling factors applied to accommodate differences between the sheet-normal and sheet curves. Shear stresses are determined through interpolation across six shear components, which are treated as independent, simplifying the process. These stresses and the constitutive matrix (C) contribute to a decoupled mechanical response, ensuring that loading in one material direction does not induce deformation in the other two directions. To handle incompressibility, a penalty method is integrated, allowing for coupling effects. Several numerical simulations were performed using a 3D finite element under various loading conditions to validate the computational model before applying it to left ventricle deformation.

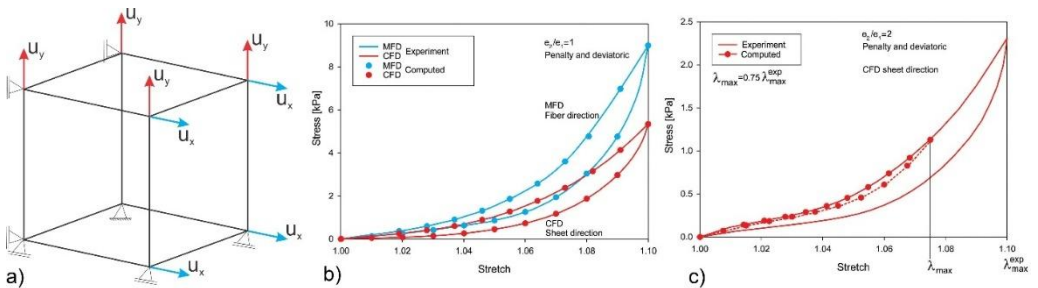


Fig. 5. (a) A 3D finite element with applied displacements, used for modeling material stretch.

Fibers align with the x-axis (MFD), while the y and z axes represent the sheet (CFD) and normal directions, respectively. The element dimensions are standardized. (b) Comparison of computed and experimental stress-stretch curves, with loading conditions corresponding to strain ratios $e_2/e_1 = 1$ and $e_2/e_1 = 2$, as used in experiments. (c) Computed constitutive relations demonstrating reduced hysteresis effects (according to Kojic et al., 2021).

The first computational experiment involved biaxial loading, where prescribed stretches were applied. The numerical results were obtained using a simplified 3D element with constrained displacements in the x and y directions (Figure 5a), ensuring a consistent strain ratio throughout the cycle. Solutions were derived through a penalty formulation, with all tested cases demonstrating a close match between numerical results and experimental stress-strain curves. As shown in Kojic et al. (2018), the implemented numerical procedure within the PAK code yields strong agreement with measured constitutive curves. The second example examined

biaxial loading conditions, but with stretches reaching only 75% of the maximum experimental curve values. This simulation specifically analyzed the case of $e_2/e_1 = 2$, applying controlled stretch levels. In a third scenario, shear deformations were introduced, replicating FS mode conditions from Holzapfel's experiments. The reverse loading followed the last unloading curve reached during the loading regime, employing a scaling factor akin to the approach used in the stretch-based simulations (Kojic et al., 2021, Figure 5c). Another key investigation involved comparing 3D finite element models with shell/membrane models to assess the consistency of tissue deformation characteristics. The analysis revealed strong agreement between the two modeling approaches, offering further insights into heart tissue behavior (Kojic et al., 2022, Figure 7.4.3).

4. Coupled electro-mechanical computational model

This example demonstrates the application of our KTM (smeared model) in simulating both the electrical potential and mechanical response of heart tissue. Calcium plays a critical role in facilitating the biochemical cycle responsible for conformational changes in muscle fiber molecules, ultimately converting chemical energy into mechanical force. Therefore, any computational model of muscle mechanics must incorporate calcium concentration variations within muscle cells over time. Our model is based on a well-established relationship from Hunter et al. (1998), which has been widely adopted (e.g., Lafortune et al., 2012; Kojic et al., 2021):

$$\sigma_{act} = \frac{[Ca^{2+}]^n}{[Ca^{2+}]^n + C_{50}^n} \sigma_{max} [1 + \eta(\lambda - 1)] \quad (3)$$

where σ_{act} represents active stress along the fiber, Ca^{2+} denotes calcium concentration, σ_{max} corresponds to the maximum isometric stress, C_{50}^n is the calcium concentration required for 50% of actin sites to be available for crossbridge binding, and η is a parameter influencing the muscle fiber deformation rate. The fiber stretch is denoted as λ . To assess the accuracy of our CSFE model, we selected a small sample of heart wall tissue based on available data (Santiago, 2018; Blausen Medical, 2014).

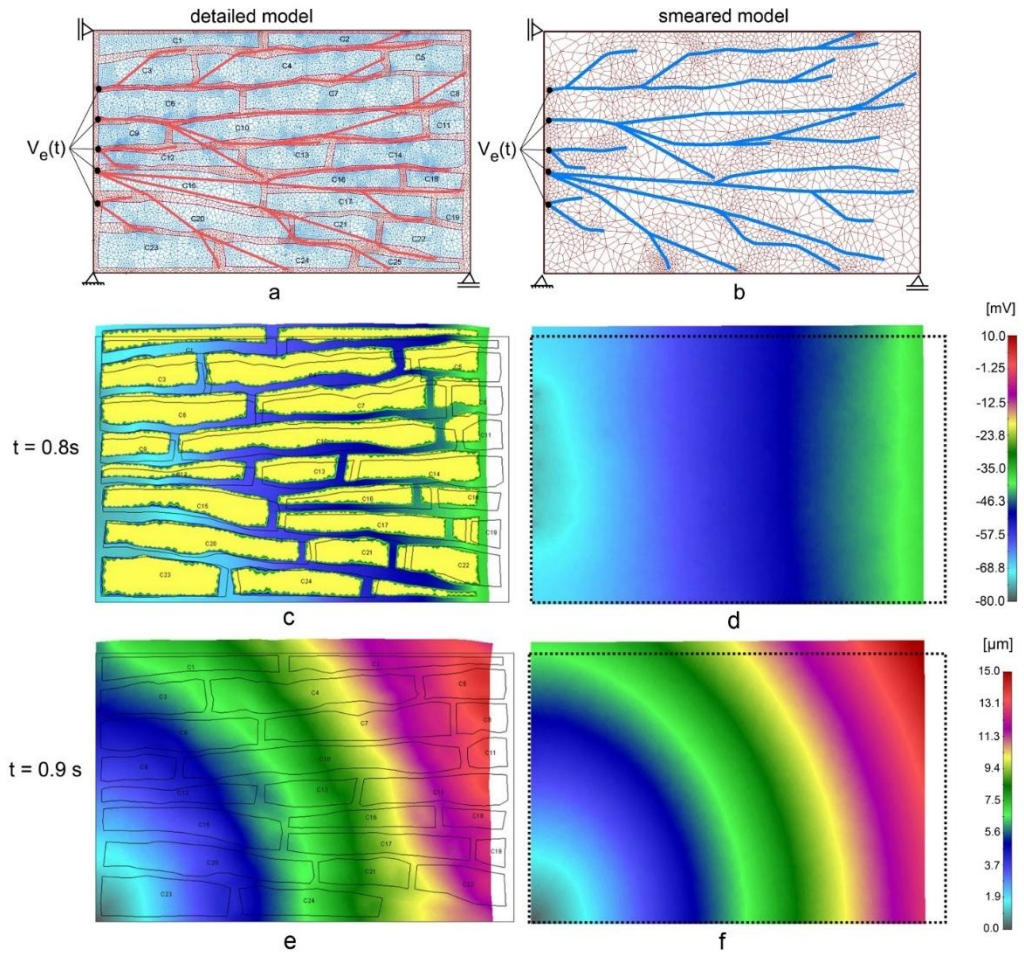


Fig. 6. (a) A detailed heart wall model including muscle cells and a Purkinje fiber network. (b) A smeared model incorporating both tissue and cells, with Purkinje fibers linked to CSFE nodes. (c) The distribution of electric potential in the detailed model and within the extracellular space of the smeared model. (d) The distribution at $t = 0.8s$. (e) Effective contractions (displacements) derived from both the detailed and smeared models. (f) The displacement field at $t = 0.9s$ (according to Kojic et al., 2019)

For further analysis, we extracted the outermost myocardial muscle layer near the sub-endocardium—an area containing Purkinje fibers. Based on available imaging data, we constructed a high-resolution 2D model consisting of a 1D mesh of Purkinje fibers and a grid of 25 cells, Figure 6a. A smeared model was then developed from this detailed representation to compute electrical potential, calcium current, and concentration following (O'Hara et al., 2011), Figure 6b. The governing function for the electric potential was derived from (Noble, 1962) and consists of two identical cycles prescribed at the Purkinje mesh's inlet nodes ($V_e(t)$ in Figure 8). A fixed cell potential of $V_e = -20$ mV was assumed. The accumulated membrane current density (I_{ORd}) was computed based on the ORd model (O'Hara et al., 2011) and incorporated into finite element solution procedure. Under these conditions, the temporal variation of the mean electric potential in the tissue is depicted in Figure 6c and 6d, with near-identical results for both detailed and smeared models. Key currents from the ORd model affecting intracellular calcium

(Ca^{2+}) concentration include: sarcolemmal Ca^{2+} pump current I_{pCa} , background Ca^{2+} current I_{Cab} , $\text{Na}^+/\text{Ca}^{2+}$ exchange current $I_{NaCa,i}$ while those influencing subspace calcium Ca^{2+} levels include L-type Ca^{2+} current I_{CaL} and $\text{Na}^+/\text{Ca}^{2+}$ exchange current $I_{NaCa,ss}$. The mean current I_{Ca} governing calcium Ca^{2+} ion transport is computed as follows (O'Hara et al., 2011):

$$I_{Ca} = -\left(I_{pCa} + I_{Cab} - 2 \cdot I_{NaCa,i}\right) \frac{V_{myo}}{V_{myo} + V_{ss}} - \left(I_{CaL} - 2 \cdot I_{NaCa,ss}\right) \frac{V_{ss}}{V_{myo} + V_{ss}} \quad (4)$$

where V_{myo} and V_{ss} denote the myoplasmic and subspace compartment volumes, respectively. The mean intracellular calcium concentration, $[Ca^{2+}]_{mean}$, is determined as the average across four compartments: myoplasmic (i), subspace (ss), network sarcoplasmic reticulum (nsr), and junctional sarcoplasmic reticulum (jsr), using the relation from (O'Hara et al., 2011):

$$[Ca^{2+}]_{mean} = \left([Ca^{2+}]_i \cdot V_{myo} + [Ca^{2+}]_{ss} \cdot V_{ss} + [Ca^{2+}]_{nsr} \cdot V_{nsr} + [Ca^{2+}]_{jsr} \cdot V_{jsr}\right) / V_{cell} \quad (5)$$

where $V_{myo} = 0.68 V_{cell}$, $V_{ss} = 0.02 V_{cell}$, $V_{nsr} = 0.0552 V_{cell}$ and $V_{jsr} = 0.048 V_{cell}$ represent respective compartmental concentrations. The detailed calculations for individual compartments follow equations provided in the Supplementary material of (O'Hara et al., 2011). Figures 6c and 6d depict the extracellular electric field potential at $t = 0.8s$ for both models, while Figures 6e and 6f show the effective contraction (magnitude of displacement vector) at $t = 0.9s$ for the first cycle of the applied electric potential. The ability to compute membrane potential from the electric field potential within the Purkinje network, extracellular space, and cellular interior enables the simulation of calcium concentration variations in muscle cells.

4. Coupling wall motion and blood flow

To accurately model heart mechanics, it is essential to couple the solid domain of the heart wall with the surrounding blood flow. The finite element balance equations for the solid domain, expressed in terms of velocity, are detailed in (Kojic et al., 2022), along with corresponding equations for the fluid domain. The fundamental coupling condition ensures that velocities at the shared boundary (between the heart wall and the blood domain) remain consistent. Two computational models were developed using this methodology: a simplified parametric model of the left ventricle and a model reconstructed from echocardiographic data. The first model represents a parametric parabolic left ventricle (LV), illustrated in Figure 7a, incorporating distinct anatomical regions such as the base, mitral valve, aortic valve, and connecting segments. Fluid-structure interaction within the PAK software is managed using a strong coupling technique. The LV wall is constrained at the base to prevent displacement and rotation, while a prescribed velocity profile is applied at the mitral valve during diastole. Figure 7b shows velocity fields at two distinct time points: 0.1s after diastole onset and 0.8s during mid-systole. The comparison of 3D and shell/membrane models demonstrates minimal discrepancy in the computed solutions.

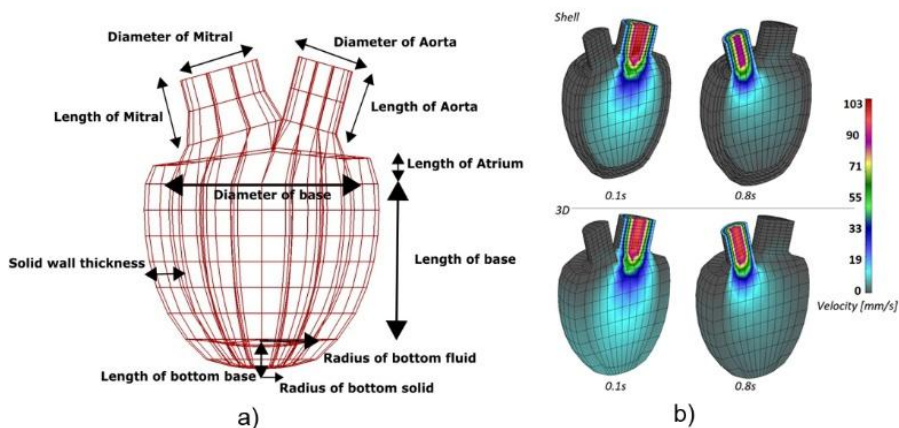


Fig. 7. (a) Geometric representation of the simplified left ventricle model with key structural components. (b) Velocity fields of the blood flow at 0.1s (early diastole) and 0.8s (mid-systole), comparing results obtained from shell/membrane and 3D models (according to Kojic et al., 2021).

The second model is based on real physiological data obtained from echocardiographic imaging, as shown in Figure 8. The finite element model was generated from echocardiographic recordings collected in a clinical setting, offering a more accurate representation of LV mechanics during a cardiac cycle (Kojic et al., 2021). The 3D LV wall model was created by extracting the internal surface geometry following the procedure described in (Kojic et al., 2021). The myocardial fiber architecture was represented using a helicoidal distribution, with fiber angles ranging from -60° at the epicardium to $+60^\circ$ at the endocardium relative to the circumferential direction. Figure 8b presents displacement fields and stress distributions along a selected external wall segment at the end of diastole when LV volume reaches its maximum. Finally, fluid flow patterns were computed based on echocardiographic recordings, further validating the methodology and offering valuable insights into LV mechanics (Kojic et al., 2021).

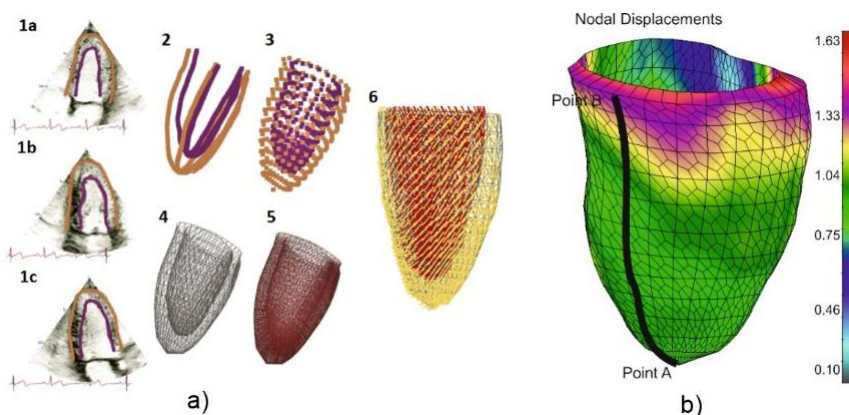


Fig. 8. a) Stepwise reconstruction of the left ventricle model from echocardiographic data. (1a, 1b, 1c) Extraction of contour lines from cross-sectional images at 90° , 150° , and 210° . (2) 3D spatial reconstruction of the contours. (3) Point distribution at the epicardium and endocardium. (4) Formation of surface elements. (5) Finite element mesh generation for the ventricular wall in its initial configuration. (6) Fiber orientation mapping. a) Displacement field on the outer ventricular wall at $t = 0.6s$, marking the end of diastole (according to Kojic et al., 2021).

4. Summary and concluding remarks

This paper has been dedicated to computational modeling of the heart. An overview of cardiac physiology was first provided to establish a foundation for the presented models. The electrophysiology section outlined fundamental principles followed by a discussion on traditional computational methods. We then presented our smeared field methodology (KTM) for electrostatics problems, comparing its effectiveness with conventional approaches through numerical simulations. The section on heart mechanics introduced finite element modeling approaches, covering both standard 3D models and a specialized shell/membrane-based FE model tailored to the unique structural properties of cardiac tissue. A finite element computational framework for modeling the mechanical behavior of the left ventricular wall by incorporating experimentally derived constitutive relationships is described in detail. One critical aspect was the coupling of stress-strain relationships for normal components, which we handled by either enforcing material incompressibility through a penalty method or incorporating a compressibility law derived from experimental observations. The accuracy of the proposed computational approach was validated through a series of test cases. Another key aspect was the development of a procedure to generate a 3D finite element mesh of the left ventricle wall using echocardiographic data. The proposed methodology was tested on representative numerical examples and applied to both a simplified parametric left ventricle model and a more physiologically accurate model reconstructed from echocardiographic data. The findings presented in this study demonstrate the potential of integrating experimental data with advanced computational models to improve the accuracy of cardiac simulations. Future work will focus on refining these models to enhance patient-specific simulations and further investigating the interplay between electrophysiology and mechanical behavior in the heart. These advancements will contribute to the development of more precise diagnostic and therapeutic tools in cardiovascular medicine.

This paper represents a summary of our research in this field in the last few years and is devoted to the celebration of 50 years of the development and application of the FE software PAK.

Acknowledgements This research was supported by the EU SILICOFCM project, Horizon 2020 research and innovation programme, grant agreement No 777204, PI Professor Nenad Filipovic; by grant number F-134 (Serbian Academy of Sciences and Arts), by the Ministry of Science, Technological Development and Innovations of the Republic of Serbia (contract number 451-03-136/2025-03/200378). The authors are also thankful the City of Kragujevac, Serbia.

References

- Bathe, K. 1996. Finite Element Procedures. Prentice-Hall, Englewood Cliffs, New Jersey, USA.
- Blausenmedical 2014. Medical gallery of Blausen Medical. WikiJournal of Medicine, 1, doi: 10.15347/wjm/2014.010.
- Geroski, V., Milosevic, M., Simic, V., Milicevic, B., Filipovic, N., Kojic, M., 2020. Composite smeared finite elementdapplication to electrical field. In: Filipovic, P.N. (Ed.), Computational Bioengineering and Bioinformatics. Springer International Publishing.
- Holzapfel, G. A., Ogden, R. W. 2009. Constitutive modelling of passive myocardium: a structurally based framework for material characterization. Phil.Trans. Roy. Soc A, 367, 3445-3475.

- Hunter, P. J., McCulloch, A. D., Ter Keurs, H. 1998. Modelling the mechanical properties of cardiac muscle. *Prog. Bioph. Molec. Biol.*, 69, 289-331.
- Kim, N., Cannell, M. B., Hunter, P. J. 2010. Changes in the calcium current among different transmural regions contributes to action potential heterogeneity in rat heart. *Prog. Bioph. Molec. Biol.*, 103, 28-34.
- Kojic, M., Bathe, K.-J. 2005. *Inelastic analysis of solids and structures*, Springer.
- Kojic, M., Milosevic, M., Simic, V., Geroski, V., Ziemys, A., Filipovic, N., Ferrari, M. 2019a. Smeared multiscale finite element model for electrophysiology and ionic transport in biological tissue. *Comp. Biol. Medicine*, 108, 288-304.
- Kojic, M., Milosevic, M., Simic, V., Milicevic, B., Geroski, V., Nizzero, S., Ziemys, A., Filipovic, N., Ferrari, M. 2019b. Smeared multiscale finite element models for mass transport and electrophysiology coupled to muscle mechanics. *Frontiers Bioeng. Biotech.*, 7, 381.
- Kojic, M., Milosevic, M., Milicevic, B., Geroski, V., Simic, V., Trifunovic, D., Stankovic, G., Filipovic, N. 2021. Computational model for heart tissue with direct use of experimental constitutive relationships. *J. Serb. Soc. Comput. Mech.*, 15, 1-23.
- Kojić, M., Milosević, M., Ziemys A. (2022), *Computational Models in Biomedical Engineering - Finite element models based on the smeared physical fields: Theory, solutions, and software*. Academic Press, Elsevier.
- Lafortune, P., Aris, R., Vázquez, M., Houzeaux, G. 2012. Coupled electromechanical model of the heart: Parallel finite element formulation. *Int. J. Numer. Meth. Biomed. Engng.*, 28, 72–86.
- Maxwell Equations [Online], 2012. Available: <https://www.maxwells-equations.com/>.
- McEvoy, E., Holzapfel, G. A., McGarry, P. 2018. Compressibility and anisotropy of the ventricular myocardium: experimental analysis and microstructural modeling. *J. Biomech. Engng.*, 140
- Mijailovich, S. M., Stojanovic, B., Kojic, M., Liang, A., Wedeen, V. J., Gilbert, R. J. 2010. Derivation of a finite-element model of lingual deformation during swallowing from the mechanics of mesoscale myofiber tracts obtained by MRI. *J. Appl. Physiology*, 109, 1500-1514.
- Noble, D. 1962. A modification of the Hodgkin-Huxley equations applicable to Purkinje fibre action and pace-maker potentials. *J. Physiology*, 160, 317-352.
- O'Hara, T., Virág, L., Varró, A., Rudy, Y. 2011. Simulation of the undiseased human cardiac ventricular action potential: Model formulation and experimental validation. *PLoS Comput. Biol.*, 7, e1002061-e1002090.
- Santiago, A. 2018. *Fluid-Electro-Mechanical Model of the Human Heart for Supercomputers*. Ph.D., Universitat Politècnica de Catalunya, Barcelona.
- Sommer, G., Haspinger, D. C., Andra, M., Sacherer, M., Viertler, C., Regiting, P., Holzapfel, G. A. 2015a. Quantification of shear deformations and corresponding stresses in the biaxially tested human myocardium. *Annals Biom. EngRG* (2015), DOI: 10.1007/s10439-015-1281-z.
- Sommer, G., Schriefl, A. J., Andrä, M., Sacherer, M., Viertler, C., Wolinski, H., Holzapfel, G. A. 2015b. Biomechanical properties and microstructure of human ventricular myocardium. *Acta biomaterialia*, 24, 172-192.
- Stevens, C., Remme, E., Legrice, I., Hunter, P. 2003. Ventricular mechanics in diastole: material parameter sensitivity. *J. Biomechanics*, 36, 737-748.
- Zipser, D. P., Jalife, J., Stevenson, W. G. Eds. 2018. *Cardiac Electrophysiology*, 7th Edition. From Cell to Bedside, Elsevier.
- Winslow, R.L., 1992. *Theoretical Foundations of Neural Modeling*, BME 580.681. The John Hopkins Univ. Sch. Medicine and Whiting Sch Engrg, Baltimore ([Google Scholar]).